Consistent evaporation formulation for the phase-field lattice Boltzmann method

Makoto Sugimoto , Yuta Sawada , Masayuki Kaneda,[*] and Kazuhiko Suga

Department of Mechanical Engineering, Osaka Prefecture University, Osaka 599-8531, Japan

A consistent evaporation model is developed for the conservative Allen-Cahn-based phase-field lattice Boltzmann method that uses an appropriate source term to recover the advection-diffusion equation for the specific humidity. To evaluate the accuracy of the proposed scheme, simulations are conducted of a steady-state one-dimensional Stefan flow for a flat interface and a three-dimensional evaporating sessile droplet on a flat substrate for a curved interface. It is confirmed that the results for the evaporative mass flux of the Stefan flow agree well with those obtained from the analytical solution within a specific humidity range of 0.8 or less at the liquid-gas interface. For the sessile droplet case, the results for the dependence of the contact angle on the evaporative mass flux and its profile show good agreement with those obtained from the model of Hu and Larson [J. Phys. Chem. B **106**, 1334 (2002)].

I. INTRODUCTION

A droplet that is deposited on a surface evaporates over time. If this droplet contains a nonvolatile solute, the shape of the final solute film that is formed depends on a variety of factors. This phenomenon is applied in inkjet printing, which is a promising method for controlled deposition of polymers on paper and functional materials on substrates such as organic semiconductor materials and transistors [1,2].

Droplet evaporation on a flat surface can occur by three different scenarios. In the first scenario, the droplet's contact line recedes at a constant contact angle. In the second scenario, the droplet's contact line is pinned and the contact angle decreases. The third scenario involves a mixture of the first two.

During evaporation, various flows are induced inside the droplet by buoyancy and by surface tension differences. Additionally, a compensating flow is induced to normalize the solute concentration if a solute is present in the liquid [3]. These internal flows and evaporation processes are the factors that govern the resulting film shape. Because the film shape is crucial for the function of the film, numerous investigations have been conducted into control of the evaporation process and the internal flows [4–7].

One of the major factors that controls the film shape is the evaporation process. The film shape is known to change from dotlike to ringlike when the evaporation rate is increased [8]. Cazabat and Guéna [9] also reviewed the evaporation processes of macroscopic sessile droplets with internal flow.

As mentioned earlier, droplet deposition methods have been applied widely. The deposition targets range from simple flat surfaces to more complex fibrous materials. Accurate prediction of the resulting film shapes on both flat surfaces and more complex structures requires use of heat and fluid flow simulation tools that can consider a variety of physical

properties, including the evaporation process and the target structures. Numerical simulations of evaporating droplets have been carried out by many researchers. Schlottke and Weigand [10] studied the evaporative flux in the volume fraction equation using the piecewise linear interface construction volume-of-fluid (PLIC-VOF) method. Hu and Larson [11] modeled the evaporative flux and investigated a shrinking sessile droplet numerically using the finite-element method (FEM). They verified that the model results agreed with the theoretical results presented by Lebedev [12] and by Picknett and Bexon [13]. Their droplet evaporation model has since become a standard benchmark.

These previous numerical works were based on use of the Navier-Stokes equation. Recently, the lattice Boltzmann method (LBM) has been attracting attention for use as an alternative computational fluid dynamics solver. The LBM offers exclusive features that include parallelization and computation on supercomputers and the ability to capture complex geometries. This method has been extended to enable its use in multiphase flow solvers such as the color-gradient model [14], the pseudopotential model (Shan-Chen model) [15], and the free-energy model [16]. For droplet simulation, however, spurious velocities presented a major drawback. In addition, only limited density and viscosity ratios were available for the multiphase LBM simulations. However, Lee [17] proposed a phase-field model that used a two-distribution-function LBE method developed from the pressure evolution equation and successfully eliminated these drawbacks. To model the droplet contact line dynamics on partially wetting surfaces, Lee and Liu [18] used Lee's method for incompressible binary fluids. In this work, they used the Cahn-Hilliard equation for the phase transport equation. Recently, the conservative Allen-Cahn equation [19,20] has come under the spotlight. While the Cahn-Hilliard equation includes a fourth-order spatial derivative in the diffusion term, the diffusion terms of the conservative Allen-Cahn equation are second-order derivatives. Therefore, the conservative Allen-Cahn equation is more robust than the Cahn-Hilliard equation at high density ratio

simulations [21]. Liang *et al.* [22] presented stable computations of the impact of a droplet on a thin liquid film with a density ratio of 1000. Their model was used in simulations of a droplet that infiltrates into porous media by Sugimoto *et al.* [23].

Phase-field LBMs have also been proposed to simulate evaporation phenomena. Ledesma-Aguilar *et al.* [24] focused on the fact that the diffusion term of the Cahn-Hilliard equation reduces to Fick's law in the limit of weak deviations from equilibrium. They simulated the evaporation of a planar film and a spherical droplet by manipulating the order parameter at the boundary to give a chemical potential gradient. Safari *et al.* [25] developed a model based on the Cahn-Hilliard phase-field LBM proposed by Lee [17] that considered the phase change with the temperature gradient used as a source term. Their model was applied to condensation in a cryogenic tube by Hatani *et al.* [26], and two-phase flow inside hot porous media by Latifiyan *et al.* [27]. Safari *et al.* [28] extended their previous model to apply to arbitrary temperature fields by including the gradient of the specific humidity at the liquid-gas interface as the driving force for evaporation. Their model has been applied to bubble growth during pool boiling by Sadeghi *et al.* [29]. However, Safari *et al.* [28] reported that the phase transfer in the steady-state one-dimensional Stefan flow simulation became less accurate when discretized using the LBM rather than the finite-difference method (FDM). In addition, these works all used the Cahn-Hilliard equation for the phase transport.

As Safari *et al.* [28] suggested, the source term for the phase transport equation should be reflected appropriately in the lattice Boltzmann equation (LBE) to improve the evaporation flux. They introduced the effect of evaporation by using a continuity equation that includes the effect of the phase change at the diffuse interface instead of a continuity equation for incompressible fluids. In their model, vapor production at the liquid-gas interface is given by the Dirichlet boundary condition with constant specific humidity. Therefore, it is suggested that the effect of evaporation at the diffuse interface must be removed from the advection-diffusion equation for the specific humidity. However, they have not completely eliminated this effect in their formulation of the LBE. This inconsistency between the governing equation and the LBE causes the overestimation of the evaporative mass flux at the liquid-gas interface. Therefore, in this study, a consistent evaporation formulation for the LBE is developed by using an appropriate source term to recover the advection-diffusion equation for the specific humidity. Additionally, to provide stable computation at the high density ratio mentioned previously by Liang *et al.* [22], the conservative Allen-Cahn equation is used as the phase transport equation in this study. Following a detailed formulation of the model, the developed model is validated further by applying it to an analysis of steady-state one-dimensional Stefan flow for a flat interface and a three-dimensional evaporating sessile droplet on a flat substrate for a curved interface.

II. GOVERNING EQUATIONS

In this section, the evaporation effect is introduced into the conservative Allen-Cahn-based phase-field model proposed by Liang *et al.* [22]. In the current phase-field model, the liquid and gas phases are distinguished using the order parameter ϕ, which is defined as a local liquid volume fraction. Therefore, ϕ takes values of 0 and 1 for the gas and liquid phases, respectively. The region where $0 < \phi < 1$ denotes a diffuse interface with finite thickness W. The local densities of the two phases are represented by

$$\tilde{\rho}_l = \phi \rho_l, \quad \tilde{\rho}_g = (1 - \phi)\rho_g, \tag{1}$$

where the subscripts l and g denote the liquid phase and the gas phase including vapor, respectively. In addition, ρ_l and ρ_g denote the bulk densities of these two phases, respectively. The gas density ρ_g is computed using the sum of the dry air density ρ_a and the vapor density (volumetric humidity) ρ_v as follows:

$$\rho_g = \rho_a + \rho_v = \frac{\rho_a}{1 - Y_v}, \tag{2}$$

where Y_v is the specific humidity (vapor mass fraction). The local averaged density is given by

$$\rho = \phi \rho_l + (1 - \phi)\rho_g. \tag{3}$$

The continuity equations for the liquid and gas phases, which include the contribution of the evaporative mass flow rate per unit volume across the liquid-gas interface $\dot{m}'''$, are given by [25,30]

$$\frac{\partial \tilde{\rho}_l}{\partial t} + \nabla \cdot (\tilde{\rho}_l \mathbf{u}) = \nabla \cdot (\rho_l \mathbf{j}_l) - \dot{m}''', \tag{4}$$

$$\frac{\partial \tilde{\rho}_g}{\partial t} + \nabla \cdot (\tilde{\rho}_g \mathbf{u}) = \nabla \cdot (\rho_g \mathbf{j}_g) + \dot{m}''', \tag{5}$$

where $\mathbf{j} = \mathbf{j}_l = -\mathbf{j}_g$ represents the flux density, which can be divided into the diffusive flux density $\mathbf{j}_D$ and the phase separation flux density $\mathbf{j}_S$ as follows [20]:

$$\mathbf{j} = \mathbf{j}_D + \mathbf{j}_S, \tag{6}$$

$$\mathbf{j}_D = M_\phi \nabla \phi, \quad \mathbf{j}_S = -M_\phi \lambda \mathbf{n}, \tag{7}$$

where M_ϕ is the mobility, $\lambda = 4\phi(1 - \phi)/W$, and $\mathbf{n} = \nabla \phi / |\nabla \phi|$ is the unit vector oriented normal to the liquid-gas interface. By substituting Eqs. (6) and (7) into Eq. (4), the conservative Allen-Cahn equation that includes consideration of evaporation is derived as follows:

$$\frac{\partial \phi}{\partial t} + \nabla \cdot (\phi \mathbf{u}) = \nabla \cdot [M_\phi (\nabla \phi - \lambda \mathbf{n})] - \frac{\dot{m}'''}{\rho_l}. \tag{8}$$

In the diffuse interface, by assuming that the gas density ρ_g is constant, Eq. (5) can be recast as

$$-\frac{\partial \phi}{\partial t} + \nabla \cdot [(1 - \phi)\mathbf{u}] = \nabla \cdot \mathbf{j}_g + \frac{\dot{m}'''}{\rho_{g,I}}, \tag{9}$$

where $\rho_{g,I}$ is the gas density at the liquid-gas interface, which is a constant. Summation of Eqs. (8) and (9) allows the new continuity equation that considers evaporation to be obtained as follows:

$$\nabla \cdot \mathbf{u} = \dot{m}''' \left(\frac{1}{\rho_{g,I}} - \frac{1}{\rho_l} \right). \tag{10}$$

The evaporative mass flow rate per unit volume $\dot{m}'''$ is calculated using the following equation [28]:

$$\dot{m}''' = \frac{\rho_{g,1}D}{1 - Y_v}\nabla Y_v \cdot \nabla\phi, \tag{11}$$

where D is the vapor diffusion coefficient in the gas phase. Note that in the region located away from the diffuse interface, the continuity equation given as Eq. (10) approaches the continuity equation for incompressible flows, $\nabla \cdot \mathbf{u} = 0$.

The Navier-Stokes equation can be written as

$$\frac{\partial(\rho\mathbf{u})}{\partial t} + \nabla \cdot (\rho\mathbf{u}\mathbf{u}) = -\nabla p + \nabla \cdot [\mu(\nabla\mathbf{u} + \nabla\mathbf{u}^{\mathrm{T}})] + \mathbf{F}, \tag{12}$$

where $\mathbf{F}$ denotes the total force term, which can be divided into the surface tension force $\mathbf{F}_s$ and the possible body force $\mathbf{F}_b$:

$$\mathbf{F} = \mathbf{F}_s + \mathbf{F}_b. \tag{13}$$

In this study, the following potential form is used for the surface tension force:

$$\mathbf{F}_s = \mu_\phi\nabla\phi, \tag{14}$$

where μ_ϕ is the chemical potential, which is defined as [31]

$$\mu_\phi = 4\beta\phi(\phi - 1)\left(\phi - \tfrac{1}{2}\right) - \kappa\nabla^2\phi, \tag{15}$$

where β and κ are the physical parameters below, which are dependent on both the interfacial thickness W and the surface tension σ:

$$\beta = \frac{12\sigma}{W}, \quad \kappa = \frac{3}{2}\sigma W. \tag{16}$$

In the scheme proposed in this work, to enable calculation of the evaporative mass flow rate per unit volume described by Eq. (11), the advection-diffusion of the vapor is only simulated in the gas phase. The advection-diffusion equation for the specific humidity can be written as [28]

$$\frac{\partial Y_v}{\partial t} + \nabla \cdot (Y_v\mathbf{u}) = \nabla \cdot (D\nabla Y_v). \tag{17}$$

In this study, the specific humidity Y_v is only defined in the gas phase ($\phi \leqslant 0.5$), and the specific humidity Y_v at the physical liquid-gas interface ($\phi = 0.5$) is fixed using the Dirichlet boundary condition. Because the vapor generation at the liquid-gas interface is only represented by the boundary condition, it is necessary to eliminate the effect of evaporation at the diffuse interface from the advection-diffusion equation. Therefore, in this study, the continuity equation for incompressible flows, $\nabla \cdot \mathbf{u} = 0$, is substituted into the advection term of Eq. (17) rather than Eq. (10), and Eq. (17) can then be recast as [28]

$$\frac{\partial Y_v}{\partial t} + \mathbf{u} \cdot \nabla Y_v = \nabla \cdot (D\nabla Y_v). \tag{18}$$

III. NUMERICAL SCHEMES

A. Lattice Boltzmann method

In this section, the governing equations are converted into LBEs. The consistency between the governing equations and these LBEs is discussed in detail in Appendix. The conservative Allen-Cahn equation, the Navier-Stokes equation, and the advection-diffusion equation for the specific humidity are converted into the following LBEs, respectively:

$$f_i(\mathbf{x} + \mathbf{e}_i\delta_t, t + \delta_t) - f_i(\mathbf{x}, t) = \Omega_i^f(\mathbf{x}, t) + \delta_t R_i^f(\mathbf{x}, t), \tag{19}$$

$$g_i(\mathbf{x} + \mathbf{e}_i\delta_t, t + \delta_t) - g_i(\mathbf{x}, t) = \Omega_i^g(\mathbf{x}, t) + \delta_t R_i^g(\mathbf{x}, t), \tag{20}$$

$$h_i(\mathbf{x} + \mathbf{e}_i\delta_t, t + \delta_t) - h_i(\mathbf{x}, t) = \Omega_i^h(\mathbf{x}, t) + \delta_t R_i^h(\mathbf{x}, t), \tag{21}$$

where f_i, g_i, and h_i are the distribution functions of the order parameter ϕ, the velocity $\mathbf{u}$, and the specific humidity Y_v, respectively. Ω_i^f, Ω_i^g, and Ω_i^h are the collision operators. R_i^f and R_i^h are the source terms, and R_i^g is the force term. The subscript i indicates the discrete direction, $\mathbf{e}_i$ is the discrete velocity, and δ_t is the time step.

In this study, the single-relaxation-time (SRT) model [32] is used for the LBE of the specific humidity distribution function h_i, and the weighted multiple-relaxation-time (WMRT) model [33] is used to form the LBEs of the order parameter and the velocity distribution functions f_i and g_i, which all require higher numerical stability. Therefore, the collision operators Ω_i^f, Ω_i^g, and Ω_i^h are described using the following equations:

$$\mathbf{\Omega}^f = -\mathbf{M}^{-1}\mathbf{S}^f\mathbf{M}(\mathbf{f} - \mathbf{f}^{\mathrm{eq}}), \tag{22}$$

$$\mathbf{\Omega}^g = -\mathbf{M}^{-1}\mathbf{S}^g\mathbf{M}(\mathbf{g} - \mathbf{g}^{\mathrm{eq}}), \tag{23}$$

$$\mathbf{\Omega}^h = -\frac{1}{\tau_h}(\mathbf{h} - \mathbf{h}^{\mathrm{eq}}), \tag{24}$$

where the superscript "eq" denotes the local equilibrium distribution function, and $\mathbf{M}$ denotes the transformation matrix of the WMRT model [33]. $\mathbf{S}^f$ and $\mathbf{S}^g$ are the diagonal collision matrices and are given as follows [33]:

$$\mathbf{S}^f = \mathrm{diag}(1, \underbrace{s_f, s_f, s_f}_{d}, \underbrace{1, 1, \ldots, 1}_{q-d-1}), \tag{25}$$

$$\mathbf{S}^g = \mathrm{diag}(\underbrace{1, 1, 1, 1}_{d+1}, \underbrace{s_g, s_g, s_g, s_g, s_g}_{(d+2)(d-1)/2}, \underbrace{1, 1, \ldots, 1}_{q-d(d+3)/2}), \tag{26}$$

where $s_f = 1/\tau_f$ and $s_g = 1/\tau_g$. d and q denote the dimension of the discrete velocity model and the number of discrete directions, respectively. The relaxation times τ_f, τ_g, and τ_h have the following relationships with the mobility M_ϕ, the kinematic viscosity ν, and the vapor diffusion coefficient D, respectively:

$$M_\phi = c_s^2\left(\tau_f - \tfrac{1}{2}\right)\delta_t, \tag{27}$$

$$\nu = c_s^2\left(\tau_g - \tfrac{1}{2}\right)\delta_t, \tag{28}$$

$$D = c_s^2\left(\tau_h - \tfrac{1}{2}\right)\delta_t, \tag{29}$$

where c_s denotes the speed of sound.

The local equilibrium distribution functions f_i^{eq} and h_i^{eq} are obtained as follows using the first-order term of the Maxwell distribution:

$$f_i^{\text{eq}} = w_i \phi \left(1 + \frac{\mathbf{e}_i \cdot \mathbf{u}}{c_s^2} \right), \tag{30}$$

$$h_i^{\text{eq}} = w_i Y_v \left(1 + \frac{\mathbf{e}_i \cdot \mathbf{u}}{c_s^2} \right). \tag{31}$$

The local equilibrium distribution function g_i^{eq} is written as [22,34]

$$g_i^{\text{eq}} = \begin{cases} \frac{p}{c_s^2}(w_i - 1) + \rho s_i(\mathbf{u}) & (i = 0), \\ \frac{p}{c_s^2} w_i + \rho s_i(\mathbf{u}) & (i \neq 0), \end{cases} \tag{32}$$

where w_i is the weight coefficient and $i = 0$ is the discrete direction in which $\mathbf{e}_i = \mathbf{0}$. s_i is the following function:

$$s_i(\mathbf{u}) = w_i \left[\frac{\mathbf{e}_i \cdot \mathbf{u}}{c_s^2} + \frac{(\mathbf{e}_i \cdot \mathbf{u})^2}{2c_s^4} - \frac{\mathbf{u} \cdot \mathbf{u}}{2c_s^2} \right]. \tag{33}$$

The source terms R_i^f and R_i^h and the force term R_i^g are required to recover the governing equations from the LBEs and are expressed as follows [21,33]:

$$\mathbf{R}^f = \mathbf{M}^{-1} \left(\mathbf{I} - \frac{\mathbf{S}^f}{2} \right) \mathbf{M} \overline{\mathbf{R}}^f, \tag{34}$$

$$\mathbf{R}^g = \mathbf{M}^{-1} \left(\mathbf{I} - \frac{\mathbf{S}^g}{2} \right) \mathbf{M} \overline{\mathbf{R}}^g, \tag{35}$$

$$\mathbf{R}^h = \left(1 - \frac{1}{2\tau_h} \right) \overline{\mathbf{R}}^h, \tag{36}$$

where

$$\overline{R}_i^f = w_i \left[\frac{\mathbf{e}_i \cdot \left\{ \partial_t (\phi \mathbf{u}) + c_s^2 \lambda \mathbf{n} \right\}}{c_s^2} - \frac{\dot{m}'''}{\rho_l} \right], \tag{37}$$

$$\overline{R}_i^g = w_i \left[\frac{\mathbf{e}_i \cdot \mathbf{F} + (\mathbf{e}_i \cdot \mathbf{u})(\mathbf{e}_i \cdot \nabla \rho)}{c_s^2} + \rho \dot{m}''' \left(\frac{1}{\rho_{g,I}} - \frac{1}{\rho_l} \right) \right], \tag{38}$$

$$\overline{R}_i^h = w_i \left[\frac{\mathbf{e}_i \cdot \left\{ \partial_t (Y_v \mathbf{u}) \right\}}{c_s^2} + Y_v \dot{m}''' \left(\frac{1}{\rho_{g,I}} - \frac{1}{\rho_l} \right) \right], \tag{39}$$

where the second term on the right-hand side of Eq. (39) is an additional term used to eliminate the effect of evaporation from the diffuse interface. In this study, the time derivative terms in Eqs. (37) and (39) above are computed using the following explicit Euler scheme [22]:

$$\partial_t (\varphi \mathbf{u}) = \frac{\varphi(t) \mathbf{u}(t) - \varphi(t - \delta_t) \mathbf{u}(t - \delta_t)}{\delta_t}, \tag{40}$$

where $\varphi = \phi$, and Y_v is a placeholder.

The macroscopic variables, comprising the order parameter ϕ, the velocity $\mathbf{u}$, the specific humidity Y_v, and the pressure p, are computed using the zeroth or first moments of the distribution functions as follows:

$$\phi = \sum_i f_i - \frac{\delta_t}{2} \frac{\dot{m}'''}{\rho_l}, \tag{41}$$

$$\mathbf{u} = \frac{1}{\rho} \left[\sum_i \mathbf{e}_i g_i + \frac{\delta_t}{2} \mathbf{F} \right], \tag{42}$$

$$Y_v = \left[1 - \frac{\delta_t}{2} \dot{m}''' \left(\frac{1}{\rho_{g,I}} - \frac{1}{\rho_l} \right) \right]^{-1} \sum_i h_i, \tag{43}$$

$$p = \frac{c_s^2}{1 - w_0} \left[\sum_{i \neq 0} g_i + \rho s_0(\mathbf{u}) + \frac{\delta_t}{2} \left\{ \mathbf{u} \cdot \nabla \rho \right. \right.$$
$$\left. \left. + (1 - w_0) \rho \dot{m}''' \left(\frac{1}{\rho_{g,I}} - \frac{1}{\rho_l} \right) \right\} \right]. \tag{44}$$

Furthermore, the kinematic viscosity ν is interpolated using the order parameter as follows:

$$\nu = \phi \nu_l + (1 - \phi) \nu_g, \tag{45}$$

where ν_l and ν_g are the kinematic viscosities of the liquid and the gas, respectively. In this study, ν_g is assumed to remain constant, regardless of the humidity. Equations (41) and (43) indicate that the evaporative mass flow rate per unit volume $\dot{m}'''$ is required to calculate the macroscopic variables. However, the order parameter ϕ and the specific humidity Y_v are required to calculate $\dot{m}'''$ using Eq. (11), thus meaning that an implicit method is required to calculate Eqs. (41) and (43) strictly. In this study, because steady flow simulations are performed, the need for an implicit method is avoided by using $\dot{m}'''$ from the previous time step to calculate Eqs. (41) and (43).

In this study, the D3Q19 and D3Q27 discrete velocity models are used for the specific humidity distribution function and the other distribution functions, respectively. Table I lists the speed of sound c_s, the discrete velocity $\mathbf{e}_i$, and the weight coefficient w_i in these models; additionally, $c = \delta_x / \delta_t$, where δ_x is the lattice spacing.

B. Refilling of the specific humidity distribution function

Because the advection-diffusion of the specific humidity Y_v is only simulated in the gas phase ($\phi \leqslant 0.5$), refilling of the specific humidity distribution function h_i is required at the grid points where the phase changes from liquid to the gas phase when the order parameter ϕ is updated. In this study, the specific humidity distribution function h_i is refilled using the following equation [35]:

$$h_i(\mathbf{x}) = h_i^{\text{eq}}(\mathbf{x}; \overline{Y_v}, \mathbf{u}_I) + h_i^{\text{neq}}(\mathbf{x} + \mathbf{e}_n \delta_t), \tag{46}$$

where $\overline{Y_v}$ is the average specific humidity at the adjacent fluid nodes before refilling, $\mathbf{u}_I$ is the velocity at the liquid-gas interface, and $\mathbf{e}_n$ denotes the discrete velocity $\mathbf{e}_i$, which has a minimum value of $\mathbf{e}_i \cdot \mathbf{n}$. In addition, $h_i^{\text{neq}} = h_i - h_i^{\text{eq}}$ denotes the nonequilibrium distribution function.

TABLE I. Parameters of the discrete velocity models.

Model	c_s/c	$\mathbf{e}_i/c$	w_i
D3Q19	$1/\sqrt{3}$	$(0, 0, 0)$	$1/3 (i = 0)$
		$(\pm 1, 0, 0), (0, \pm 1, 0), (0, 0, \pm 1)$	$1/18 (i = 1, \ldots, 6)$
		$(\pm 1, \pm 1, 0), (\pm 1, 0, \pm 1), (0, \pm 1, \pm 1)$	$1/36 (i = 7, \ldots, 18)$
D3Q27	$1/\sqrt{3}$	$(0, 0, 0)$	$8/27 (i = 0)$
		$(\pm 1, 0, 0), (0, \pm 1, 0), (0, 0, \pm 1)$	$2/27 (i = 1, \ldots, 6)$
		$(\pm 1, \pm 1, 0), (\pm 1, 0, \pm 1), (0, \pm 1, \pm 1)$	$1/54 (i = 7, \ldots, 18)$
		$(\pm 1, \pm 1, \pm 1)$	$1/216 (i = 19, \ldots, 26)$

IV. RESULTS AND DISCUSSION

A. Steady-state one-dimensional Stefan flows

To validate the evaporative mass flux at flat liquid-gas interfaces, simulations of a steady-state one-dimensional Stefan flow [28] are performed. Figure 1 shows the computational domain used for the simulations of the Stefan flow. These are the only simulations in which the motion of the liquid-gas interface is not computed using the conservative Allen-Cahn equation, and the order parameter profile is fixed using the following equation:

$$\phi(x) = \frac{1}{2}\left[1 + \tanh\frac{2(x_I - x)}{W}\right], \qquad (47)$$

where x_I is the x-coordinate of the liquid-gas interface ($\phi = 0.5$). In these simulations, the Dirichlet conditions [36,37], where $p = p_\infty$ and $Y_v = Y_{v,\infty} = 0$ at the x-direction boundaries and $Y_v = Y_{v,I}$ at the liquid-gas interface, are imposed by the half-way bounce-back (HWBB) scheme. Furthermore, periodic boundary conditions are used at the y- and z-direction boundaries. The computational domain size is set at $(2L(x), 0.02L(y), 0.02L(z))$ and the x-direction length of the gas phase is set at $L = 200\delta_x$. The parameters used for the simulations are the density ratio $\rho_l/\rho_a = 856$, the viscosity ratio $\mu_l/\mu_g = 55$, and the Schmidt number of the vapor $\mathrm{Sc} = \nu_g/D = 0.6$. The specific humidity at the liquid-gas interface is varied over the $0.1 \leqslant Y_{v,I} \leqslant 0.8$ range.

In this section, the evaporative mass flux that occurs at the liquid-gas interface $\dot{m}_I''$ is compared with the analytical solution for this flux. The evaporative mass flux $\dot{m}''$ is computed using the following equation [28]:

$$\dot{m}'' = \frac{\rho_{g,I}D}{1 - Y_v}\nabla Y_v \cdot \mathbf{n}. \qquad (48)$$

From the continuity equation at the steady-state condition $d(\rho u)/dx = 0$, the following equation is obtained:

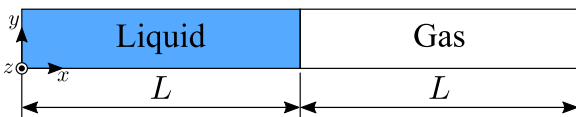$$\dot{m}''(x) = \rho u = \text{const.} \qquad (49)$$

The conservation of the vapor mass in the gas phase can be written as [28]

$$\dot{m}_I'' = Y_v\dot{m}_I'' - \rho_{g,I}D\frac{dY_v}{dx}. \qquad (50)$$

By integrating Eq. (50) with the assumption of $\rho_{g,I}D = \text{const}$ and applying two boundary conditions as

$$Y_v|_{x=x_I=L} = Y_{v,I}, \qquad Y_v|_{x=2L} = Y_{v,\infty}, \qquad (51)$$

one can derive the analytical solution as follows [28]:

$$\dot{m}_I'' = \frac{\rho_{g,I}D}{L}\ln\left(\frac{1 - Y_{v,\infty}}{1 - Y_{v,I}}\right). \qquad (52)$$

Figure 2 shows the nondimensional evaporative mass flux $\dot{m}_I''/(\rho_{g,I}D/L)$ varying with the specific humidity at the liquid-gas interface $Y_{v,I}$. In this section, $\dot{m}_I''/(\rho_{g,I}D/L)$ is calculated via linear extrapolation because the liquid-gas interface is placed at the midpoint of the grid points. The solid line represents the analytical solution determined using Eq. (52). The red circles and green triangles show the results produced using the proposed scheme and the conventional scheme that was presented by Safari et al. [28], respectively. The blue squares show the results determined using the scheme in which the source terms that contain $\dot{m}'''$ in Eqs. (39) and (43) are not introduced, i.e., the scheme in which the LBE of h_i is used to recover Eq. (17). Figure 2 confirms that the scheme without the source terms (blue squares) overestimates the evaporative mass flux in a manner similar to the scheme developed by Safari et al. [28] (green triangles). In contrast, because the appropriate source terms were used in the LBE of h_i to recover Eq. (18), the proposed scheme reproduced the analytical solution with greater accuracy.

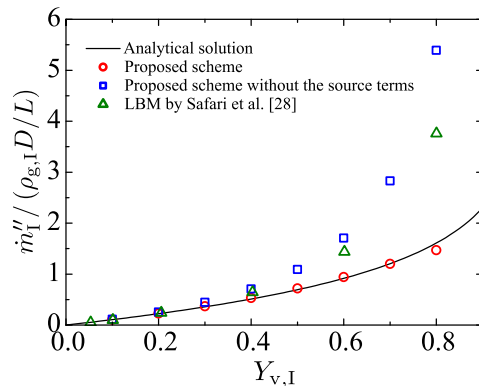FIG. 1. Computational domain used for the simulations of the Stefan flows.

FIG. 2. Nondimensional evaporative mass flux in the simulations of the Stefan flows.
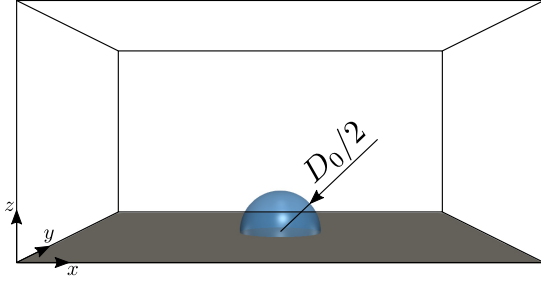
FIG. 3. Schematic of the computational domain used for the simulations of the evaporating droplet on the flat substrate.

B. Evaporation of a droplet on a flat substrate

To validate the evaporative mass flux obtained at the droplet surface, simulations of a three-dimensional evaporating droplet on a flat substrate are performed. Figure 3 shows a schematic drawing of the computational domain. In these simulations, a droplet with an initial diameter $D_0 = 40\delta_x$ is deposited at the center of a flat substrate at an initial contact angle of $\theta_0 = 90°$. The computational domain size is set to $(15D_0(x), 15D_0(y), 7.5D_0(z))$. On the substrate, the nonslip condition for the velocity and the no-flux conditions for the order parameter and the specific humidity are imposed via the HWBB scheme. Furthermore, the cubic boundary condition [38] is used to reproduce the substrate's wettability. At the computational domain boundaries, except for those on the substrate, the no-flux condition for the order parameter and the Dirichlet conditions [36,37] $p = p_\infty$ and $Y_v = Y_{v,\infty}$ are also imposed via the HWBB scheme. Furthermore, at the liquid-gas interface, the Dirichlet condition $Y_v = Y_{v,I}$ is imposed via the interpolated bounce-back (IPBB) scheme. The parameters used in the simulations are the density ratio $\rho_l/\rho_a = 856$, the viscosity ratio $\mu_l/\mu_g = 55$, the Schmidt number of the vapor $Sc = 0.6$, the Ohnesorge number $Oh = \mu_l/\sqrt{\rho_l \sigma D_0} = 3.4 \times 10^{-3}$, and the specific humidity values $Y_{v,\infty} = 0$ and $Y_{v,I} = 0.2$. In this section, the droplet is assumed to evaporate with a constant contact angle, and the three contact angles $\theta = 30°, 60°, 90°$ are simulated.

Figure 4 shows the snapshots of the specific humidity field around the droplet obtained in the simulations. The solid lines in Fig. 4 show the contour lines of the specific humidity Y_v. Figure 4 confirms that the contour lines of the specific humidity approach the hemispherical shape as the distance from the droplet increases due to the boundary condition of the bottom wall. For the evaluation of the spurious velocities in the uniform evaporation rate case, the velocity field inside the droplet at $\theta = 90°$ is shown in Fig. 5. It can be confirmed that the spurious velocity is well suppressed in terms of the velocity magnitude.

Additionally, the evaporative mass flux at the liquid-gas interface $\dot{m}_I''$ is compared with the following model equation that was proposed by Hu and Larson [11]:

$$\frac{\dot{m}_I''(r)}{\dot{m}_I''(0)} = \left[1 - \left(\frac{r}{R}\right)^2\right]^{\theta/\pi - 0.5}, \tag{53}$$

where r is the distance from the central axis of the droplet and R is the wetting radius. $\dot{m}_I''(0)$ is the evaporative mass
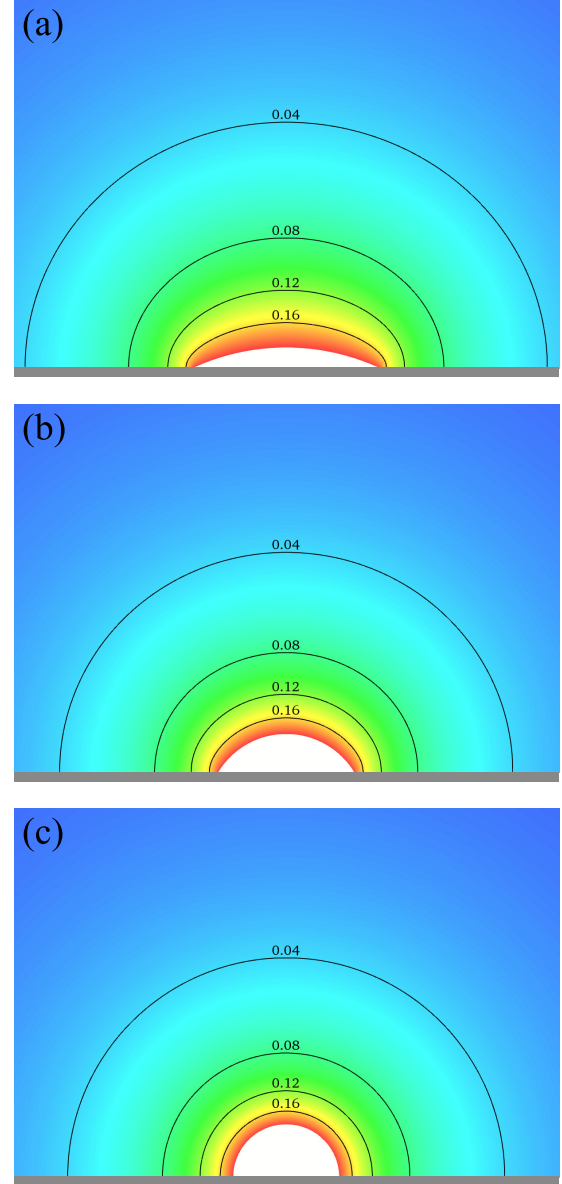

FIG. 4. Specific humidity field around the droplet obtained in the simulations of a droplet on a flat substrate at different contact angles: (a) $\theta = 30°$, (b) $\theta = 60°$, and (c) $\theta = 90°$.
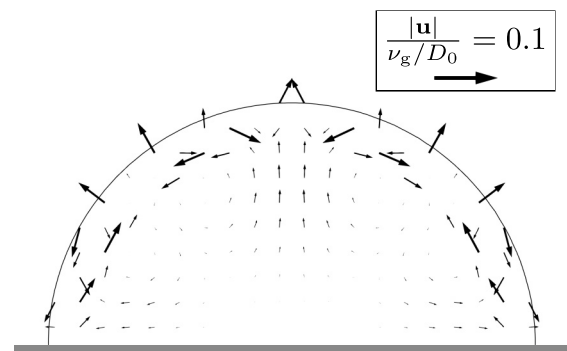

FIG. 5. Velocity field inside the droplet obtained in the simulation of a droplet on a flat substrate at $\theta = 90°$.
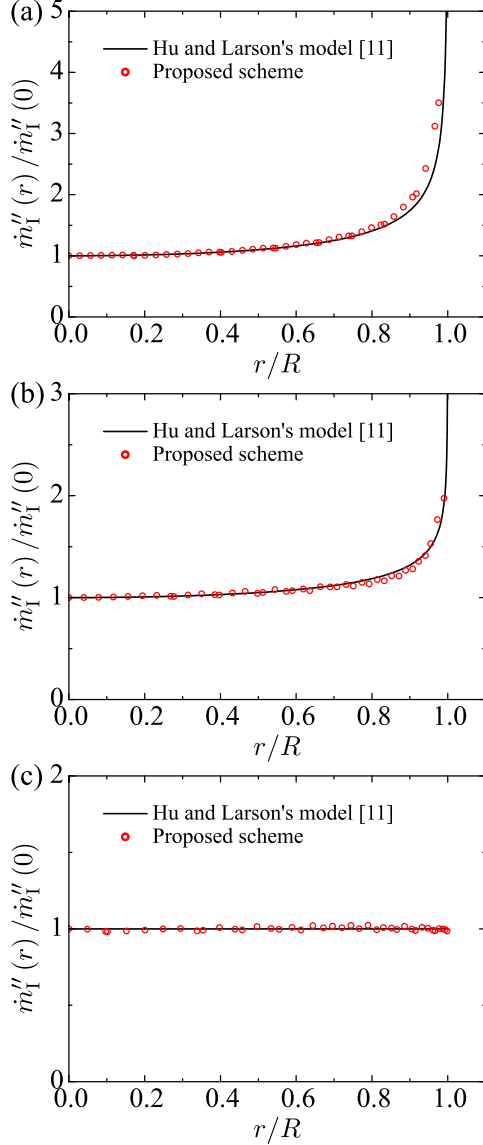
FIG. 6. Nondimensional evaporative mass flux profiles obtained in the simulations of a droplet on a flat substrate at different contact angles: (a) $\theta = 30°$, (b) $\theta = 60°$, and (c) $\theta = 90°$.

flux at the top of the droplet. In this section, $\dot{m}_I''$ is calculated via linear extrapolation at the bases of the perpendicular lines from the gas nodes adjacent to the liquid-gas interface to the interface itself. The results for the nondimensional evaporative mass flux $\dot{m}_I''(r)/\dot{m}_I''(0)$ are shown in Fig. 6. Figure 6 confirms that the proposed scheme can reproduce the nondimensional evaporative mass flux profiles produced by Hu and Larson [11] with high accuracy over a broad range of contact angles.

Additionally, the absolute value of $\dot{m}_I''(0)$ is compared with the value obtained using the model equation proposed by Hu and Larson [11], which is expressed as follows:

$$\dot{m}_{I,\text{model}}''(0) = \frac{D(\rho_{v,I} - \rho_{v,\infty})}{R}(0.27\theta^2 + 1.30)$$

$$\times \left[0.6381 - 0.2239\left(\theta - \frac{\pi}{4}\right)^2\right], \quad (54)$$
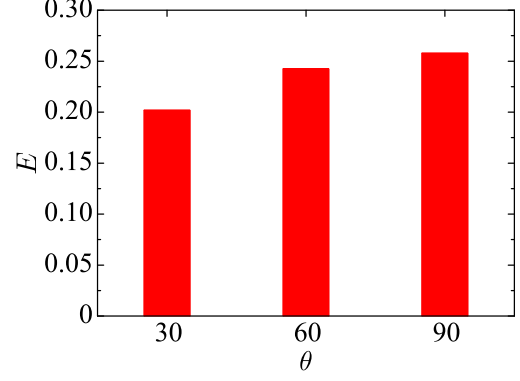

FIG. 7. Relative error of the evaporative mass flux at the top of the droplet from the model proposed by Hu and Larson [11].

where $\rho_{v,I}$ and $\rho_{v,\infty}$ are the vapor densities at the liquid-gas interface and in the ambient gas, respectively. Figure 7 shows the relative error of the evaporative mass flux at the top of the droplet obtained from the model of Hu and Larson [11], where E denotes the following relative error:

$$E = \frac{\dot{m}_I''(0) - \dot{m}_{I,\text{model}}''(0)}{\dot{m}_{I,\text{model}}''(0)}. \quad (55)$$

Figure 7 suggests that the proposed scheme estimates the evaporative mass flux to be more than 20% higher than the model. These relative errors are considered to be caused by the fact that Hu and Larson's simulations are only based on the diffusion equation of the vapor mass concentration [11], while the proposed scheme considers the advection-diffusion of the vapor in the gas phase. Indeed, in Fig. 8, the normal velocity is the highest at the droplet apex ($d/D_0 \cong 0$), which supports the contribution of the advection. In the present simulations, therefore, the evaporation is enhanced by the Stefan flow near the liquid-gas interface, which results in the higher evaporation mass flux.

V. CONCLUSION

The effect of evaporation is introduced into the phase-field LBM based on the conservative Allen-Cahn equation. By adding an appropriate source term to the LBE, the problem
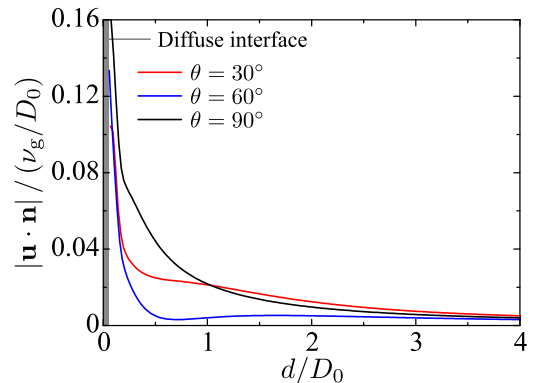

FIG. 8. Normal velocity profile from the droplet apex along the z-direction, where d denotes the distance from the droplet apex.

of overestimation of the evaporative mass flux that occurs in the conventional scheme [28] is solved. The proposed scheme is validated via simulations of a steady-state one-dimensional Stefan flow and an evaporating droplet on a flat substrate. The simulations of the steady-state one-dimensional Stefan flow confirmed that the evaporative mass flux can be reproduced using the proposed scheme with greater accuracy than the conventional scheme [28] in the region where $Y_{v,I} \leqslant 0.8$. The simulations of the evaporating droplet on the flat substrate confirmed that the model equation for the nondimensional evaporative mass flux proposed by Hu and Larson [11] can be reproduced with high accuracy over a wide contact angle range, while the proposed scheme estimates the absolute value of the evaporative mass flux at the top of the droplet to be more than 20% higher than the value obtained using the model. However, this is because Hu and Larson's simulations are only based on the diffusion equation of the vapor mass concentration [11], while the proposed scheme considers the advection-diffusion of the vapor in the gas phase.

For a diffuse-interface model such as the phase-field model, the representation of the contact angle as super-lyophilic and super-lyophobic becomes less accurate due to its thickened interface at the contact line. Although the reasonable computational parameter range is limited, the LBM enables computation in a complex physical structure, such as ink evaporation on paper and fabric, a wick in heat pipes, etc.

In this study, we focused on verifying the accuracy of the evaporative mass flux in the proposed scheme. In future work, we plan to introduce the thermal field and its effects on the evaporative mass flux and the surface tension.

APPENDIX: CHAPMAN-ENSKOG ANALYSIS

The Chapman-Enskog analysis is performed to confirm consistency between the LBEs and the governing equations. For simplicity, the SRT collision operators are used here. The distribution functions, the time and spatial derivatives, the unit vector normal to the liquid-gas interface, the evaporative mass flow rate per unit volume, and the total force are expanded in consecutive scales of ϵ as follows:

$$f_i = f_i^{(0)} + \epsilon f_i^{(1)} + \epsilon^2 f_i^{(2)} + \cdots, \tag{A1a}$$

$$g_i = g_i^{(0)} + \epsilon g_i^{(1)} + \epsilon^2 g_i^{(2)} + \cdots, \tag{A1b}$$

$$h_i = h_i^{(0)} + \epsilon h_i^{(1)} + \epsilon^2 h_i^{(2)} + \cdots, \tag{A1c}$$

$$\partial_t = \epsilon \partial_{t_1} + \epsilon^2 \partial_{t_2}, \quad \partial_\alpha = \epsilon \partial_{1\alpha}, \tag{A1d}$$

$$n_\alpha = \epsilon n_\alpha^{(1)}, \quad \dot{m}''' = \epsilon \dot{m}'''^{(1)}, \quad F_\alpha = \epsilon F_\alpha^{(1)}, \tag{A1e}$$

where ϵ is a small expansion parameter.

1. Conservative Allen-Cahn equation

Using the moments of the equilibrium distribution function and the source term, one can derive the following:

$$\sum_i f_i^{eq} = \phi, \tag{A2a}$$

$$\sum_i e_{i\alpha} f_i^{eq} = \phi u_\alpha, \tag{A2b}$$

$$\sum_i e_{i\alpha} e_{i\beta} f_i^{eq} = \phi c_s^2 \delta_{\alpha\beta}, \tag{A2c}$$

$$\sum_i \overline{R}_i^f = -\frac{\dot{m}'''}{\rho_l}, \tag{A3a}$$

$$\sum_i e_{i\alpha} \overline{R}_i^f = \partial_t(\phi u_\alpha) + c_s^2 \lambda n_\alpha, \tag{A3b}$$

where $\delta_{\alpha\beta}$ is the Kronecker delta. By applying the Taylor expansion to Eq. (19) and substituting Eqs. (A1a), (A1d), and (A1e) into this equation, the following multiscale equations can be derived:

$$\epsilon^0 : f_i^{(0)} = f_i^{eq}, \tag{A4a}$$

$$\epsilon^1 : D_{1i} f_i^{(0)} = -\frac{1}{\tau_f \delta_t} f_i^{(1)} + \left(1 - \frac{1}{2\tau_f}\right) \overline{R}_i^{f(1)}, \tag{A4b}$$

$$\epsilon^2 : \partial_{t_2} f_i^{(0)} + D_{1i} f_i^{(1)} + \frac{\delta_t}{2} D_{1i}^2 f_i^{(0)}$$
$$= -\frac{1}{\tau_f \delta_t} f_i^{(2)} + \left(1 - \frac{1}{2\tau_f}\right) \overline{R}_i^{f(2)}, \tag{A4c}$$

where $D_{1i} := \partial_{t_1} + e_{i\alpha} \partial_{1\alpha}$. By substituting Eq. (A4b) into Eq. (A4c), one can then derive

$$\partial_{t_2} f_i^{(0)} + D_{1i}\left[\left(1 - \frac{1}{2\tau_f}\right)\left(f_i^{(1)} + \frac{\delta_t}{2}\overline{R}_i^{f(1)}\right)\right]$$
$$= -\frac{1}{\tau_f \delta_t} f_i^{(2)} + \left(1 - \frac{1}{2\tau_f}\right)\overline{R}_i^{f(2)}. \tag{A5}$$

In a manner similar to Liang *et al.* [34], to remove the implicitness of the LBE, the order parameter distribution function f_i is defined using the form that includes the source term. Therefore, the zeroth moment of f_i can be derived as follows:

$$\sum_i f_i = \sum_i f_i^{eq} - \frac{\delta_t}{2}\sum_i \overline{R}_i^f = \phi + \frac{\delta_t}{2}\frac{\dot{m}'''}{\rho_l}. \tag{A6}$$

Equation (41) can easily be obtained from Eq. (A6), and by applying a multiscale expansion to Eq. (A6), the following equations can be obtained:

$$\sum_i f_i^{(1)} = \frac{\delta_t}{2}\frac{\dot{m}'''^{(1)}}{\rho_l}, \tag{A7a}$$

$$\sum_i f_i^{(n)} = 0 \ (n \geqslant 2). \tag{A7b}$$

By summing Eqs. (A4b) and (A5) over i, the following equations can be recovered, respectively:

$$\partial_{t_1}\phi + \partial_{1\alpha}(\phi u_\alpha) = -\frac{\dot{m}'''^{(1)}}{\rho_l}, \tag{A8}$$

$$\partial_{t_2}\phi + \partial_{1\alpha}\left[\left(1 - \frac{1}{2\tau_f}\right)\left(\sum_i e_{i\alpha}f_i^{(1)} + \frac{\delta_t}{2}\sum_i e_{i\alpha}\overline{R}_i^{f(1)}\right)\right] = 0.$$
(A9)

Use of Eq. (A4b) allows the summation terms in Eq. (A9) to be recast as

$$\sum_i e_{i\alpha}f_i^{(1)} + \frac{\delta_t}{2}\sum_i e_{i\alpha}\overline{R}_i^{f(1)}$$

$$= -\tau_f\delta_t\left[\sum_i D_{1i}e_{i\alpha}f_i^{(0)} - \left(1 - \frac{1}{2\tau_f}\right)\sum_i e_{i\alpha}\overline{R}_i^{f(1)}\right]$$

$$+ \frac{\delta_t}{2}\sum_i e_{i\alpha}\overline{R}_i^{f(1)}$$

$$= -c_s^2\tau_f\delta_t\left(\partial_{1\alpha}\phi - \lambda n_\alpha^{(1)}\right).$$
(A10)

Substitution of Eq. (A10) into Eq. (A9) allows one to derive

$$\partial_{t_2}\phi = \partial_{1\alpha}\left[c_s^2\left(\tau_f - \frac{1}{2}\right)\delta_t\left(\partial_{1\alpha}\phi - \lambda n_\alpha^{(1)}\right)\right].$$
(A11)

By combining Eqs. (A8) and (A11) at the ϵ and ϵ^2 scales and substituting Eq. (27) into this equation, one can then derive the conservative Allen-Cahn equation with consideration of the evaporation, which is given as Eq. (8).

2. Continuity equation and Navier-Stokes equation

Using the moments of the equilibrium distribution function and the force term, one can derive the following:

$$\sum_i g_i^{\text{eq}} = 0,$$
(A12a)

$$\sum_i e_{i\alpha}g_i^{\text{eq}} = \rho u_\alpha,$$
(A12b)

$$\sum_i e_{i\alpha}e_{i\beta}g_i^{\text{eq}} = \rho u_\alpha u_\beta + p\delta_{\alpha\beta},$$
(A12c)

$$\sum_i e_{i\alpha}e_{i\beta}e_{i\gamma}g_i^{\text{eq}} = \rho c_s^2\Delta_{\alpha\beta\gamma\zeta}u_\zeta,$$
(A12d)

$$\sum_i \overline{R}_i^g = u_\gamma\partial_\gamma\rho + \rho\dot{m}'''\left(\frac{1}{\rho_{g,I}} - \frac{1}{\rho_l}\right),$$
(A13a)

$$\sum_i e_{i\alpha}\overline{R}_i^g = F_\alpha,$$
(A13b)

$$\Lambda_{\alpha\beta} := \sum_i e_{i\alpha}e_{i\beta}\overline{R}_i^g = c_s^2\left[u_\alpha\partial_\beta\rho + u_\beta\partial_\alpha\rho + \left\{u_\gamma\partial_\gamma\rho\right.\right.$$

$$\left.\left. + \rho\dot{m}'''\left(\frac{1}{\rho_{g,I}} - \frac{1}{\rho_l}\right)\right\}\delta_{\alpha\beta}\right], \quad (A13c)$$

where $\Delta_{\alpha\beta\gamma\zeta} := \delta_{\alpha\beta}\delta_{\gamma\zeta} + \delta_{\alpha\gamma}\delta_{\beta\zeta} + \delta_{\alpha\zeta}\delta_{\beta\gamma}$. By applying the Taylor expansion to Eq. (20) and substituting Eqs. (A1b), (A1d), and (A1e) into this equation, the following multiscale

equations can be derived:

$$\epsilon^0 : g_i^{(0)} = g_i^{\text{eq}},$$
(A14a)

$$\epsilon^1 : D_{1i}g_i^{(0)} = -\frac{1}{\tau_g\delta_t}g_i^{(1)} + \left(1 - \frac{1}{2\tau_g}\right)\overline{R}_i^{g(1)},$$
(A14b)

$$\epsilon^2 : \partial_{t_2}g_i^{(0)} + D_{1i}g_i^{(1)} + \frac{\delta_t}{2}D_{1i}^2g_i^{(0)} = -\frac{1}{\tau_g\delta_t}g_i^{(2)}.$$
(A14c)

By substituting Eq. (A14b) into Eq. (A14c), one can derive

$$\partial_{t_2}g_i^{(0)} + D_{1i}\left[\left(1 - \frac{1}{2\tau_g}\right)\left(g_i^{(1)} + \frac{\delta_t}{2}\overline{R}_i^{g(1)}\right)\right] = -\frac{1}{\tau_g\delta_t}g_i^{(2)}.$$
(A15)

The zeroth and first moments of g_i can be derived as [34]

$$\sum_i g_i = \sum_i g_i^{\text{eq}} - \frac{\delta_t}{2}\sum_i \overline{R}_i^g$$

$$= -\frac{\delta_t}{2}\left[u_\gamma\partial_\gamma\rho + \rho\dot{m}'''\left(\frac{1}{\rho_{g,I}} - \frac{1}{\rho_l}\right)\right], \quad (A16)$$

$$\sum_i e_{i\alpha}g_i = \sum_i e_{i\alpha}g_i^{\text{eq}} - \frac{\delta_t}{2}\sum_i e_{i\alpha}\overline{R}_i^g = \rho u_\alpha - \frac{\delta_t}{2}F_\alpha.$$
(A17)

Equations (42) and (44) can easily be obtained from Eqs. (A16) and (A17), and by applying the multiscale expansion to Eqs. (A16) and (A17), the following equations can be obtained:

$$\sum_i g_i^{(1)} = -\frac{\delta_t}{2}\left[u_\gamma\partial_{1\gamma}\rho + \rho\dot{m}'''^{(1)}\left(\frac{1}{\rho_{g,I}} - \frac{1}{\rho_l}\right)\right],$$
(A18a)

$$\sum_i g_i^{(n)} = 0, \quad (n \geqslant 2),$$
(A18b)

$$\sum_i e_{i\alpha}g_i^{(1)} = -\frac{\delta_t}{2}F_\alpha^{(1)},$$
(A18c)

$$\sum_i e_{i\alpha}g_i^{(n)} = 0, \quad (n \geqslant 2).$$
(A18d)

Summation of Eq. (A14b), Eq. (A14b)$\times e_{i\beta}$, and Eq. (A15)$\times e_{i\beta}$ over i allows the following equations to be recovered, respectively:

$$\partial_{1\alpha}u_\alpha = \dot{m}'''^{(1)}\left(\frac{1}{\rho_{g,I}} - \frac{1}{\rho_l}\right),$$
(A19)

$$\partial_{t_1}(\rho u_\beta) + \partial_{1\alpha}(\rho u_\alpha u_\beta + p\delta_{\alpha\beta}) = F_\beta^{(1)},$$
(A20)

$$\partial_{t_2}(\rho u_\beta) + \partial_{1\alpha}\left[\left(1 - \frac{1}{2\tau_g}\right)\left(\sum_i e_{i\alpha}e_{i\beta}g_i^{(1)} + \frac{\delta_t}{2}\Lambda_{\alpha\beta}^{(1)}\right)\right] = 0.$$
(A21)

By substituting Eq. (A19) into Eq. (A13c), one can then obtain

$$\Lambda_{\alpha\beta}^{(1)} = c_s^2[u_\alpha\partial_{1\beta}\rho + u_\beta\partial_{1\alpha}\rho + \partial_{1\gamma}(\rho u_\gamma)\delta_{\alpha\beta}].$$
(A22)

Using Eqs. (A14b) and (A22), the summation terms in Eq. (A21) can be recast as

$$\sum_i e_{i\alpha} e_{i\beta} g_i^{(1)} + \frac{\delta_t}{2} \Lambda_{\alpha\beta}^{(1)}$$

$$= -\tau_g \delta_t \left[\sum_i D_{1i} e_{i\alpha} e_{i\beta} g_i^{(0)} - \left(1 - \frac{1}{2\tau_g}\right) \Lambda_{\alpha\beta}^{(1)} \right]$$

$$+ \frac{\delta_t}{2} \Lambda_{\alpha\beta}^{(1)} = -\rho c_s^2 \tau_g \delta_t (\partial_{1\alpha} u_\beta + \partial_{1\beta} u_\alpha), \quad \text{(A23)}$$

where the terms for $O(\delta_t Ma^2)$ have been neglected under the incompressible limit [22]. Substitution of Eq. (A23) into Eq. (A21) allows one to derive the following:

$$\partial_{t_2} (\rho u_\beta) = \partial_{1\alpha} \left[\rho c_s^2 (\tau_g - \tfrac{1}{2}) \delta_t (\partial_{1\alpha} u_\beta + \partial_{1\beta} u_\alpha) \right]. \quad \text{(A24)}$$

Multiplication of Eq. (A19) by ϵ enables one to derive the continuity equation with consideration of evaporation that is given as Eq. (10). Additionally, by combining Eqs. (A20) and (A24) at the ϵ and ϵ^2 scales and substituting Eq. (28) into this equation, one can then derive the Navier-Stokes equation given as Eq. (12).

3. Advection-diffusion equation for the specific humidity

Using the moments of the equilibrium distribution function and the source term, one can derive the following:

$$\sum_i h_i^{\text{eq}} = Y_v, \quad \text{(A25a)}$$

$$\sum_i e_{i\alpha} h_i^{\text{eq}} = Y_v u_\alpha, \quad \text{(A25b)}$$

$$\sum_i e_{i\alpha} e_{i\beta} h_i^{\text{eq}} = Y_v c_s^2 \delta_{\alpha\beta}, \quad \text{(A25c)}$$

$$\sum_i \overline{R}_i^h = Y_v \dot{m}''' \left(\frac{1}{\rho_{g,I}} - \frac{1}{\rho_l} \right), \quad \text{(A26a)}$$

$$\sum_i e_{i\alpha} \overline{R}_i^h = \partial_t (Y_v u_\alpha). \quad \text{(A26b)}$$

By applying the Taylor expansion to Eq. (21) and substituting Eqs. (A1c), (A1d), and (A1e) into this equation, the following multiscale equations can be derived:

$$\epsilon^0 : h_i^{(0)} = h_i^{\text{eq}}, \quad \text{(A27a)}$$

$$\epsilon^1 : D_{1i} h_i^{(0)} = -\frac{1}{\tau_h \delta_t} h_i^{(1)} + \left(1 - \frac{1}{2\tau_h}\right) \overline{R}_i^{h(1)}, \quad \text{(A27b)}$$

$$\epsilon^2 : \partial_{t_2} h_i^{(0)} + D_{1i} h_i^{(1)} + \frac{\delta_t}{2} D_{1i}^2 h_i^{(0)}$$

$$= -\frac{1}{\tau_h \delta_t} h_i^{(2)} + \left(1 - \frac{1}{2\tau_h}\right) \overline{R}_i^{h(2)}. \quad \text{(A27c)}$$

By substituting Eq. (A27b) into Eq. (A27c), one can then derive

$$\partial_{t_2} h_i^{(0)} + D_{1i} \left[\left(1 - \frac{1}{2\tau_h}\right) \left(h_i^{(1)} + \frac{\delta_t}{2} \overline{R}_i^{h(1)}\right) \right]$$

$$= -\frac{1}{\tau_h \delta_t} h_i^{(2)} + \left(1 - \frac{1}{2\tau_h}\right) \overline{R}_i^{h(2)}. \quad \text{(A28)}$$

The zeroth moment of h_i can be derived as [34]

$$\sum_i h_i = \sum_i h_i^{\text{eq}} - \frac{\delta_t}{2} \sum_i \overline{R}_i^h = Y_v \left[1 - \frac{\delta_t}{2} \dot{m}''' \left(\frac{1}{\rho_{g,I}} - \frac{1}{\rho_l} \right) \right]. \quad \text{(A29)}$$

Equation (43) can easily be obtained from Eq. (A29), and by applying the multiscale expansion to Eq. (A29), the following equations can be obtained:

$$\sum_i h_i^{(1)} = -\frac{\delta_t}{2} Y_v \dot{m}'''^{(1)} \left(\frac{1}{\rho_{g,I}} - \frac{1}{\rho_l} \right), \quad \text{(A30a)}$$

$$\sum_i h_i^{(n)} = 0, \quad (n \geqslant 2). \quad \text{(A30b)}$$

By summing Eqs. (A27b) and (A28) over i, the following equations can be recovered:

$$\partial_{t_1} Y_v + \partial_{1\alpha}(Y_v u_\alpha) = Y_v \dot{m}'''^{(1)} \left(\frac{1}{\rho_{g,I}} - \frac{1}{\rho_l} \right), \quad \text{(A31)}$$

$$\partial_{t_2} Y_v + \partial_{1\alpha} \left[\left(1 - \frac{1}{2\tau_h}\right) \left(\sum_i e_{i\alpha} h_i^{(1)} + \frac{\delta_t}{2} \sum_i e_{i\alpha} \overline{R}_i^{h(1)} \right) \right] = 0. \quad \text{(A32)}$$

Using Eq. (A27b), the summation terms in Eq. (A32) can be recast as

$$\sum_i e_{i\alpha} h_i^{(1)} + \frac{\delta_t}{2} \sum_i e_{i\alpha} \overline{R}_i^{h(1)}$$

$$= -\tau_h \delta_t \left[\sum_i D_{1i} e_{i\alpha} h_i^{(0)} - \left(1 - \frac{1}{2\tau_h}\right) \sum_i e_{i\alpha} \overline{R}_i^{h(1)} \right]$$

$$+ \frac{\delta_t}{2} \sum_i e_{i\alpha} \overline{R}_i^{h(1)}$$

$$= -c_s^2 \tau_h \delta_t \partial_{1\alpha} Y_v. \quad \text{(A33)}$$

By substituting Eq. (A33) into Eq. (A32), one can derive the following:

$$\partial_{t_2} Y_v = \partial_{1\alpha} \left[c_s^2 (\tau_h - \tfrac{1}{2}) \delta_t \partial_{1\alpha} Y_v \right]. \quad \text{(A34)}$$

By combining Eqs. (A31) and (A34) at the ϵ and ϵ^2 scales and substituting Eqs. (29) and (10) into this equation, one can then derive the advection-diffusion equation for the specific humidity given as Eq. (18).

[1] J. A. Lim, J.-H. Kim, L. Qiu, W. H. Lee, H. S. Lee, D. Kwak, and K. Cho, Inkjet-printed single-droplet organic transistors based on semiconductor nanowires embedded in insulating polymers, Adv. Funct. Mater. **20**, 3292 (2010).

[2] Y. Li, L. Lan, P. Xiao, S. Sun, Z. Lin, W. Song, E. Song, P. Gao, W. Wu, and J. Peng, Coffee-ring defined short channels for inkjet-printed metal oxide thin-film transistors, ACS Appl. Mater. Interfaces **8**, 19643 (2016).

[3] R. D. Deegan, O. Bakajin, T. F. Dupont, G. Huber, S. R. Nagel, and T. A. Witten, Capillary flow as the cause of ring stains from dried liquid drops, Nature **389**, 827 (1997).

[4] K. Sefiane, Effect of nonionic surfactant on wetting behavior of an evaporating drop under a reduced pressure environment, J. Colloid Interface Sci. **272**, 411 (2004).

[5] Y. O. Popov, Evaporative deposition patterns: Spatial dimensions of the deposit, Phys. Rev. E **71**, 036313 (2005).

[6] T. Kajiya, W. Kobayashi, T. Okuzono, and M. Doi, Controlling the drying and film formation processes of polymer solution droplets with addition of small amount of surfactants, J. Phys. Chem. B **113**, 15460 (2009).

[7] Y. Yoshitake, S. Yasumatsu, M. Kaneda, K. Nakaso, and J. Fukai, Structure of circulation flows in polymer solution droplets receding on flat surfaces, Langmuir **26**, 3923 (2010).

[8] M. Kaneda, H. Ishizuka, Y. Sakai, J. Fukai, S. Yasutake, and A. Takahara, Film formation from polymer solution using inkjet printing method, AIChE J. **53**, 1100 (2007).

[9] A.-M. Cazabat and G. Guéna, Evaporation of macroscopic sessile droplets, Soft Matter **6**, 2591 (2010).

[10] J. Schlottke and B. Weigand, Direct numerical simulation of evaporating droplets, J. Comput. Phys. **227**, 5215 (2008).

[11] H. Hu and R. G. Larson, Evaporation of a sessile droplet on a substrate, J. Phys. Chem. B **106**, 1334 (2002).

[12] N. N. Lebedev, *Special Functions and Their Applications* (Prentice-Hall, Englewood Cliffs, NJ, 1965).

[13] R. Picknett and R. Bexon, The evaporation of sessile or pendant drops in still air, J. Colloid Interface Sci. **61**, 336 (1977).

[14] A. K. Gunstensen, D. H. Rothman, S. Zaleski, and G. Zanetti, Lattice Boltzmann model of immiscible fluids, Phys. Rev. A **43**, 4320 (1991).

[15] X. Shan and H. Chen, Lattice Boltzmann model for simulating flows with multiple phases and components, Phys. Rev. E **47**, 1815 (1993).

[16] M. R. Swift, E. Orlandini, W. R. Osborn, and J. M. Yeomans, Lattice Boltzmann simulations of liquid-gas and binary fluid systems, Phys. Rev. E **54**, 5041 (1996).

[17] T. Lee, Effects of incompressibility on the elimination of parasitic currents in the lattice Boltzmann equation method for binary fluids, Comput. Math. Appl. **58**, 987 (2009).

[18] T. Lee and L. Liu, Lattice Boltzmann simulations of micron-scale drop impact on dry surfaces, J. Comput. Phys. **229**, 8045 (2010).

[19] P.-H. Chiu and Y.-T. Lin, A conservative phase field method for solving incompressible two-phase flows, J. Comput. Phys. **230**, 185 (2011).

[20] M. Geier, A. Fakhari, and T. Lee, Conservative phase-field lattice Boltzmann model for interface tracking equation, Phys. Rev. E **91**, 063309 (2015).

[21] H. Wang, X. Yuan, H. Liang, Z. Chai, and B. Shi, A brief review of the phase-field-based lattice Boltzmann method for multiphase flows, Capillarity **2**, 33 (2019).

[22] H. Liang, J. Xu, J. Chen, H. Wang, Z. Chai, and B. Shi, Phase-field-based lattice Boltzmann modeling of large-density-ratio two-phase flows, Phys. Rev. E **97**, 033309 (2018).

[23] M. Sugimoto, M. Kaneda, and K. Suga, Phase-field lattice Boltzmann simulation of minute droplet onto isotropic porous media, Trans. JSME (in Japanese) **86**, 20 (2020).

[24] R. Ledesma-Aguilar, D. Vella, and J. M. Yeomans, Lattice-Boltzmann simulations of droplet evaporation, Soft Matter **10**, 8267 (2014).

[25] H. Safari, M. H. Rahimian, and M. Krafczyk, Extended lattice Boltzmann method for numerical simulation of thermal phase change in two-phase fluid flow, Phys. Rev. E **88**, 013304 (2013).

[26] M. A. Hatani, M. Farhadzadeh, and M. H. Rahimian, Investigation of vapor condensation on a flat plate and horizontal cryogenic tube using lattice Boltzmann method, Int. Commun. Heat Mass Transf. **66**, 218 (2015).

[27] N. Latifiyan, M. Farhadzadeh, P. Hanafizadeh, and M. H. Rahimian, Numerical study of droplet evaporation in contact with hot porous surface using lattice Boltzmann method, Int. Commun. Heat Mass Transf. **71**, 56 (2016).

[28] H. Safari, M. H. Rahimian, and M. Krafczyk, Consistent simulation of droplet evaporation based on the phase-field multiphase lattice Boltzmann method, Phys. Rev. E **90**, 033305 (2014).

[29] R. Sadeghi, M. S. Shadloo, M. Y. A. Jamalabadi, and A. Karimipour, A three-dimensional lattice Boltzmann model for numerical investigation of bubble growth in pool boiling, Int. Commun. Heat Mass Transf. **79**, 58 (2016).

[30] H. Ding, P. D. Spelt, and C. Shu, Diffuse interface model for incompressible two-phase flows with large density ratios, J. Comput. Phys. **226**, 2078 (2007).

[31] D. Jacqmin, Calculation of two-phase Navier-Stokes flows using phase-field modeling, J. Comput. Phys. **155**, 96 (1999).

[32] P. L. Bhatnagar, E. P. Gross, and M. Krook, A model for collision processes in gases. I. Small amplitude processes in charged and neutral one-component systems, Phys. Rev. **94**, 511 (1954).

[33] A. Fakhari, D. Bolster, and L.-S. Luo, A weighted multiple-relaxation-time lattice Boltzmann method for multiphase flows and its application to partial coalescence cascades, J. Comput. Phys. **341**, 22 (2017).

[34] H. Liang, B. C. Shi, Z. L. Guo, and Z. H. Chai, Phase-field-based multiple-relaxation-time lattice Boltzmann model for incompressible multiphase flows, Phys. Rev. E **89**, 053320 (2014).

[35] H. Gao, H. Li, and L.-P. Wang, Lattice Boltzmann simulation of turbulent flow laden with finite-size particles, Comput. Math. Appl. **65**, 194 (2013).

[36] L. Li, R. Mei, and J. F. Klausner, Boundary conditions for thermal lattice Boltzmann equation method, J. Comput. Phys. **237**, 366 (2013).

[37] L. Li, R. Mei, and J. F. Klausner, Lattice Boltzmann models for the convection-diffusion equation: D2Q5 vs D2Q9, Int. J. Heat Mass Transf. **108**, 41 (2017).

[38] L. Liu and T. Lee, Wall free energy based polynomial boundary conditions for non-ideal gas lattice Boltzmann equation, Int. J. Mod. Phys. C **20**, 1749 (2009).

[39] https://en-author-services.edanzgroup.com/.